First-Principles Characterization and Comparison of Clean, Hydrated, and Defect α-Al_2O_3 (110) Surfaces

Ali Abbaspour Tamijani, Jennifer L. Bjorklund, Jeffrey G. Catalano, Sara E. Mason*

University of Iowa, Department of Chemistry, Iowa City, Iowa 52242

Washington University, Department of Earth and Planetary Sciences, St. Louis, Missouri 63130

*corresponding author: sara-mason@uiowa.edu

Abstract

Structural models of the (110) termination of α-Al_2O_3 are studied using density functional theory (DFT) calculations and thermodynamics modeling to determine the details of the mineral-water interface structure. It has been established for other facets of both alumina and isostructural hematite that surface preparation conditions can influence the stoichiometry and structure observed during in situ experimental characterization studies. To this end, we use theory and modeling to determine the thermodynamically preferred surface structures as a function of the chemical environment, in terms of the oxygen chemical potential, pressure, and temperature. Consistent with studies of other facets of alumina, we find that thermodynamically unfavorable defect structures, upon hydration and hydroxylation, can show greater stability than the hydrated forms of ideal terminations. The model results are compared to experimental characterization of the hydrated (110) surface, with good agreement in terms of layer spacings and calculated surface-free energies. The electronic structure of the exposed surface functional groups is presented and discussed in terms of structure-reactivity concepts used in geochemical surface science.

1. Introduction

At the interface between mineral surfaces and water, a number of chemical reactions and transformations occur, influencing environmental water composition, transport and ultimate fate of pollutants, aerosol formation in the atmosphere, microbially-mediated redox processes, geological CO_2 sequestration, and environmental catalysis.[1-9] Hydration or hydroxylation of mineral surfaces results in the thermodynamic preference for surface functional groups (and arrangements thereof) that differ substantially from the structure under ultra-high vacuum (UHV) conditions.[10-15] Advances in X-ray based techniques have enabled in situ measurements of mineral-water interfaces, providing new structural and mechanistic insights into mineral-water interfaces.[1, 3-6, 16-18] In particular, a great deal of effort has been devoted to studies of specific model mineral-water interface systems, including a series of isostructural low-index alumina (α-Al_2O_3) and hematite (α-Fe_2O_3) surfaces, using a broad range of approaches.[19-26] Both minerals share an underlying bulk structure, shown in Figure 1. Differences in surface preparation conditions and measurement conditions have been shown to influence surface structure for the (001) and (012) mineral-water interfaces for both analogs.[15, 27-29] Complementary theoretical studies using an atomistic thermodynamics approach based on density functional theory (DFT) calculations on the alumina and hematite (001) and (012) hydrated aided in revealing the role of surface preparation on controlling the resulting mineral-water interface structure.[30] The utility of combined experimental and theoretical approaches to understanding transformations of mineral surfaces from UHV to ambient conditions provides a means for verifying interface structure, which is key to ultimately understanding reactivity such as partitioning reactions, sorption, and geochemical cycling of contaminants in natural waters.[31]

The reactivity of mineral-water interfaces is based on the chemical identity of the exposed oxygen functional groups. The principle of bond-valence (BV) can be used to rank surface functional group reactivity by taking into account the local coordination environment.[32-33] Such BV analysis has been particularly useful in geochemistry in forming a basis for structure-reactivity relationships of mineral-water interfaces and their sorption complexes. [23 28, 34-35] Structural characterization studies underscore that hydrated α-Al_2O_3 and α-Fe_2O_3 exhibit local coordinations of surface functional groups that vary substantially from those of the bulk terminations of the crystal. For example, the α-Al_2O_3 (001) surface in vacuum is found to be terminated by a layer of Al atoms in three-fold coordination with underlying oxygen.[36-40] When the surface is exposed to water, subsequent characterization reveals the terminal layer to be comprised of hydroxyl groups in two-fold coordination with octahedrally coordinated bulk Al atoms.[15, 40] Based on the fairly saturated bonding environment of the exposed doubly coordinated hydroxyl groups, the α-Al_2O_3 (001)-water structure is interpreted to be particularly stable and unreactive. For the (012) facet of α-Al_2O_3, the hydrated surface differs substantially from that of the (001) facet and is reported to exhibit hydroxyl groups that are singly-, doubly-, or triply-coordinated to underlying bulk Al atoms. The greater range of exposed oxygen functional groups is the basis of the molecular-level interpretation of the enhanced sorption reactivity of the (012) α-Al_2O_3-water interface relative to that of the (001).[16] Furthermore, protonation states of oxygen functional groups depend on factors such as pH, acid-base properties of the exposed oxygen groups, and other ionic species in solution. The degree of protonation controls the charge of the surface and influences interactions between the surface and ions or water molecules.[10, 34]

Figure 1. Unit cell of hexagonal corundum α-Al_2O_3, with the (110) plane shown in purple, where $a=b\neq c$. Blue and red spheres are Al and O atoms, respectively.

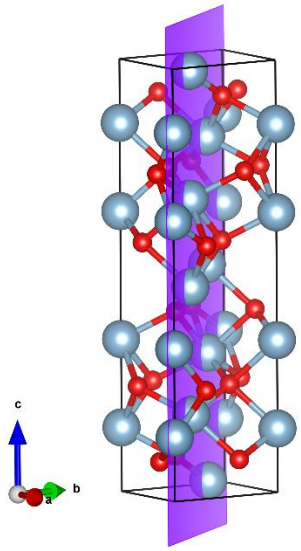

Recent in situ experimental work has characterized the α-Al_2O_3 (110)-water interface, including interfacial water ordering.[41] In this study, two surface samples were prepared; one that was annealed at 723 K and one annealed at 1373 K. The sample annealed at the lower temperature resulted in an unreconstructed, defect-free surface. The sample annealed at a higher temperature showed oscillatory patterns in the X-ray scattering data that suggested a reconstructed, defect surface formed. The best fit structural model consisted of one third of the surface oxygen and one half of the surface aluminum groups missing.

While difficult to experimentally characterize, the exposed functional groups in the defect-free structure (Figure 2) are expected to protonate in water to satisfy the bonding environment. Furthermore, the two structures reported for the hydrated (110) surface can be related in terms of the identity of the molecular fragments removed in forming the defect structure. In line with the previous study, we note that the surface can be partitioned into two distinct fragments comprised of two aluminum atoms and associated oxygen atoms, and these clusters are referred to as dimers. The (110) surface exposes two types of dimers, arranged in diagonal patterns, labeled here as Type A (purple) and Type B (green, Figure 2). The dimers can be differentiated in terms of coordination to surface oxygen functional groups. The Al atoms of Dimer A are connected to doubly- and triply-coordinated oxygen functional groups, while those of Dimer B are connected to singly- and doubly-coordinated functional groups. The best fit of the experimental structural data supports that the defect surface obtained at the higher annealing temperature is likely related to the ideal structure by the removal of Type A dimer groups.

Figure 2. Top-view of the defect-free (110) α-Al_2O_3 surface, where the four types of oxygen groups are color-coded as follows: gold for the singly-coordinated oxygen (AlO), orange for the doubly-coordinated oxygen (Al_2O), red for the triply-coordinated oxygen (Al_3O), and maroon for the bulk oxygen. The aluminum atoms are represented with small blue spheres. The two exposed dimer types are arranged in diagonal patterns, where the Type A dimer is highlighted in purple, and the Type B dimer is highlighted in green.

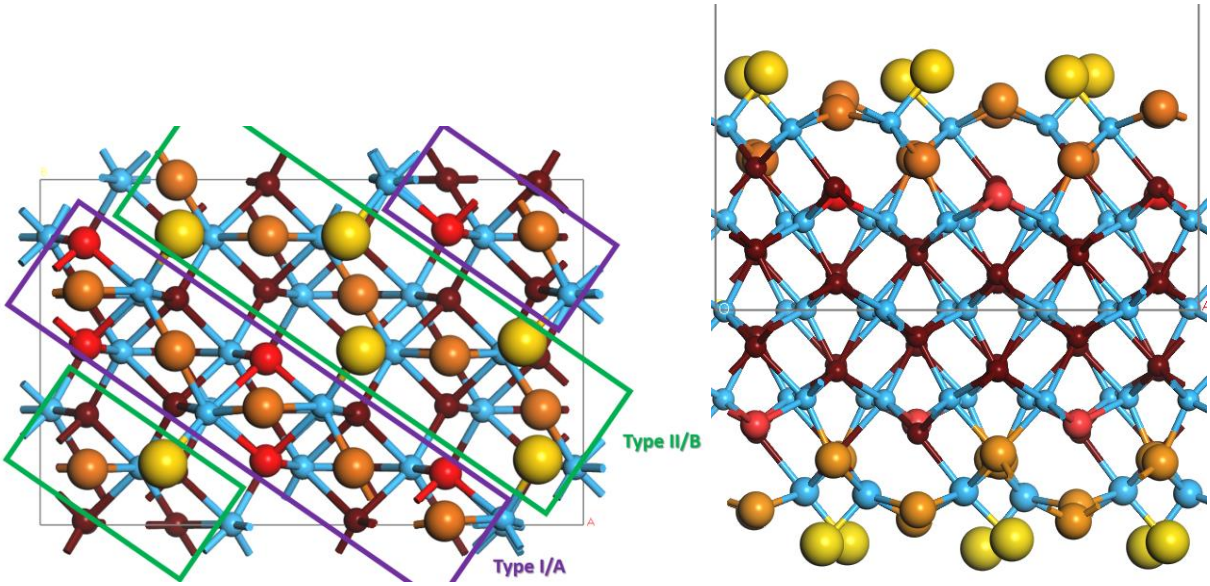

To provide further characterization of the (110)-water interface, we use DFT and ab initio thermodynamics. We are particularly interested in understanding how the surface-free energy, geometry, and electronic structure are influenced by hydration effects. To this end, we study model surfaces that span oxygen terminations and their hydroxylated forms, including surface defects. We are able to assess the relative stability of the exposed surfaces as a function of oxygen chemical potential, which can be related to finite temperature and pressure conditions. The structural models investigated here include ones that are commensurate with those from prior in situ experimental work and go on to include a range of hypothetical structures to form a basis of comparison. We present ab initio thermodynamics phase diagrams, details of the optimized surface geometries, and aspects of electronic structure to provide theoretical characterization complementary to reported experimental X-ray reflectivity and atomic force microscopy measurements.

2. Methodology & Computational Details

2.1. Density Functional Theory Calculations

Periodic Density Functional Theory (DFT)[42-43] calculations were carried out as implemented within the Quantum Espresso (QE) open source package at the GGA-PBE level, using GBRV ultra-soft pseudopotentials.[27, 44-46] Based on the requirements of the employed pseudopotentials, a plane-wave cutoff of 40 Ry for the wavefunction and 320 Ry for the charge density is used to expand the Kohn-Sham orbitals. All atoms were allowed to fully relax during geometry optimizations of bulk and slab systems, using a force convergence threshold of 0.005 eV/Å^2 per atom. For bulk calculations, a (4 × 4 × 4) Monkhorst-Pack *k*-point grid was selected based on convergence studies of the total energy.[47] The DFT-optimized bulk α-Al_2O_3 lattice parameters were *a* = 4.817 Å (-1.09%) and *c* = 13.143 Å (-1.03%), in excellent agreement with the experimental data and previously DFT values .[48-49]

The optimized bulk structure was then cleaved along the (110) plane to generate a *P*1 surface cell consistent with that defined in prior work [Figure 2]. The surface cell was used to form structural slab models by adding 25 Å of vacuum between the periodic images along the *c* crystallographic axis, which was found to minimize the interaction between neighboring repeats. The resulting surface slab dimensions are 13.14×8.34×4.27 $Å^3$, for which a (2 × 4 × 1) *k*-point grid was determined to achieve energy convergence. The thickness of the slabs was tested against calculated surface energy and a six Al-layered slab was selected, resulting in a total slab height of 12.94 Å for the pristine surface, as shown in Figure 2. All slab models generated exhibit inversion symmetry such that the top and bottom exposed surfaces are identical, and are subject to geometry optimizations without constraint in line with previously determined best practices.[50-52]

2.2. Ab initio Thermodynamics

An ab initio thermodynamic approach was used, as described in detail by Reuter and Scheffler [52-54] and as implemented for α-Al_2O_3 surfaces by Mason et al.[28] The utility of the approach is to compare the thermodynamic stability of various surface stoichiometries through computed values of surface-free energy. The surface-free energy (γ) can be expressed in terms of the difference between the Gibbs free energy of the slab and the summation over all the chemical potentials of individual species multiplied by their atomic count:

$$\gamma(T,p,N_i) = \frac{1}{2A}\{G_{\text{slab}}(T,p,N_i) - \sum_i N_i \mu_i(T,p)\} \cdot \quad (3)$$

In equation (3), G_{slab} is the Gibbs free energy of the periodic slab; A is the surface area of the slab; N_i is the number of particles of species i; and μ_i denotes the chemical potential of the species i. The factor $\frac{1}{2}$ takes into account the two equivalent surfaces in the symmetric slab models. The finite temperature and pressure of the system are accounted for in the chemical potentials. The temperature and pressure dependence of the chemical potential for gaseous particles is formulated as:

$$\mu_i(T,p) = \mu_i\left(T,p^\circ\right) + \frac{1}{2}k_{\text{B}}Tln\left(\frac{p}{p^\circ}\right) \cdot \quad (4)$$

Tabulated values [55] are used to identify the temperature-dependent chemical potentials under standard pressure conditions (termed as $\mu_i\left(T,p^\circ\right)$). The finite-pressure dependent chemical potential term ($\mu_i(T,p)$) is determined using equation (4).

Although the vibrational motions do not contribute significantly to the surface-free energy in O-terminated structures [53], it has been demonstrated that such effects cannot be neglected for H-terminated surfaces [28]. The vibrational contribution to the free energy was included by calculating the phonon frequencies for hydrated surfaces. Vibrational analysis was carried out based on DFT calculations using Quantum Espresso and the open-source python-based Phonopy program.[56] This software package applies a frozen phonon approach to compute forces and frequencies. The calculations were done using a ±0.01 Å displacement imposed on the DFT-optimized structures. To maintain consistency in the calculations, all single-point energy calculations were repeated using the same convergence criteria as for the relaxed calculations. Zero-point energy correction terms were calculated using these lattice vibrational frequencies. The computed vibrational frequencies were used to calculate the vibrational partition function q_{vib}.

It is noted that in the thermodynamics approach, the surfaces of variable stoichiometry are assumed to be in equilibrium with both bulk α-Al_2O_3 and gas-phase species. Thus, chemical potential is defined in a range of rich and poor limits. Accordingly, a range of surface-free energies is obtained that span the zone between lower- and upper-limits for the chemical potential of O (i.e. μ_O). Owing to well-known errors in DFT-GGA atomization energies,[46] we apply an empirical correction to the DFT value of the O_2 total energy.[28, 57]

2.3. (110) Surface Models

We generate structural models for the α-Al_2O_3 (110) surface that fall under 3 headings: Oxygen-Terminated, Hydrated Ideal, and Hydrated Defect. The Oxygen-Terminated class represents surface terminations that would result from cleavage along the (110) plane, followed by additional removal of surface oxygen until a charge-neutral slab results. The Hydrated Ideal class is comprised of structures in which dangling bonds in polar structures resulting from direct cleavage along the (110) plane are capped with hydrogen to achieve charge neutrality. Structures under this class span the best fit model for the unreconstructed, hydrated surface prepared by lower temperature annealing in the prior experimental study on this surface, as well as additional hypothetical possibilities. The Hydrated Defect class represents models in which Al dimer groups have been removed, followed by the addition of hydrogen to cap dangling bonds. This group is meant to represent the experimental reconstructed surface resulting from higher temperature annealing based on the (110) experimental study and other models based on distinct defect types. By spanning these nine distinct surface terminations, we are able to assess the relative stability with and without hydration effects. Outside of the three structure categories, we identify one aluminum terminated surface, referred to as Al-term (110) that is charge-neutral based on formal charges. As detailed later, this structure is high in energy and therefore included only for comparison. To compare stability as a function of surface fact, we also include the oxygen-terminated A1 cut of (012) and aluminum-terminated (001) surfaces, as detailed in previous studies.[28, 58] Figure S1 of the Supporting Information shows side views of these surfaces.

The bulk layer sequencing and occupancy numbers for the (110) surface in the *P*1 cell is O_6-O_3-O_3-O_6-Al_{12}-*R*, where *R* represents the bulk repeat unit. All of the surfaces modeled in the current work are derived from this parent stoichiometry, with *X* used to denote a missing layer. The details of the model surface stoichiometries are given in Table 1, and all are designed to be charge-neutral based on ideal formal oxidation states. Our nomenclature is such that a defect-free surface is labeled as Perfect, while models with missing layers are labeled as Defect. This label is then followed by –O (–H) based on the surface termination, where in the –H termination an index number of 1 or 2 is used to denote different hydration schemes. In hydration scheme 1, all exposed oxygen functional groups are assigned one hydrogen atom, while in scheme 2 aquo groups are considered for comparison. In both schemes, the amount of hydrogen is constant. It is useful to explore the different hydration schemes as the protonation state of exposed oxygen functional groups, a key reactivity factor, cannot be determined directly by experiment.

Figure 3. Side views of the optimized Oxygen-Terminated surface models. Solid orange lines correspond to doubly-coordinated oxygen functional group layers (Al_2O); dashed red lines correspond to triply-coordinated oxygen functional group layers (Al_3O); dotted blue and maroon lines correspond to aluminum and bulk-like oxygen lower layers, respectively.

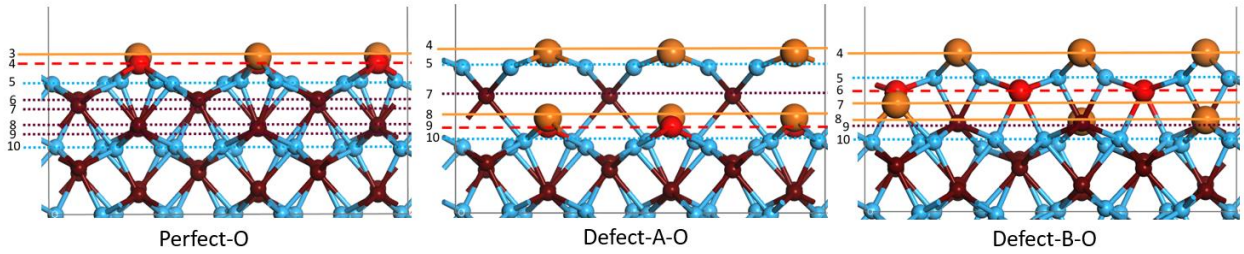

i. Oxygen-Terminated Surfaces

The three oxygen terminated surface models are shown in Figure 3. Unlike the (001) or (012) surface planes, there are no terminations from a (110) cleavage of α-Al_2O_3 that result directly in a nonpolar surface. Therefore, to maintain charge-neutral surface slabs, different layers of oxygen are removed from each of the oxygen-terminated structures. The Perfect-O surface is missing the two top-most layers, resulting in a layer sequencing of X_6-X_3-O_3-O_6-Al_{12}-*R*. By the same token, Defect-A-O and Defect-B-O have stacking sequences of X_6-X_3-X_3-O_6-Al_6-X_6-O_3-O_3-Al_{12}-*R*, and X_6-X_3-O_3-X_6-Al_6-O_6-X_3-O_3-O_6-Al_{12}-*R*, respectively. Layers of oxygen and half of a layer of aluminum are removed to generate the two defect structure types in the form of Al_2O_3 units to create the Defect-A-O and Defect-B-O surfaces. For example, Defect-A-O is missing the L6 oxygen layer, leaving three layers of oxygen between aluminum layers L5 and L10. Defect-B-O is comparatively missing less layers of oxygen with all four layers in between the two labeled aluminum layers.

Table 1. Surface models for clean and hydrated (110) plane of α-Al_2O_3. Indices are the occupancies at each layer.

	Layer sequencing for modeled terminations											
Model	*i*	1	2	3	4	5	6	7	8	9	10	
Oxygen-Terminated												
Perfect-O	-	X	X	O_3	O_6	Al_{12}	O_6	O_3	O_3	O_6	Al_{12}	*R*
Defect-A-O	-	X	X	X	O_6	Al_6	X	O_3	O_3	O_6	Al_{12}	*R*
Defect-B-O	-	X	X	O_3	X	Al_6	O_6	X	O_3	O_6	Al_{12}	*R*
Hydrated Ideal												
Perfect-H1	H1	O_6	O_3	O_3	O_6	Al_{12}	O_6	O_3	O_3	O_6	Al_{12}	*R*
Perfect-H2	H2	O_6	O_3	O_3	O_6	Al_{12}	O_6	O_3	O_3	O_6	Al_{12}	*R*
Hydrated Defect												
Defect-A-H1	H1	O_6	X	X	O_6	Al_6	O_6	O_3	O_3	O_6	Al_{12}	*R*
Defect-A-H2	H2	O_6	X	X	O_6	Al_6	O_6	O_3	O_3	O_6	Al_{12}	*R*
Defect-B-H1	H1	X	O_3	O_3	O_6	Al_6	O_6	O_3	O_3	O_6	Al_{12}	*R*
Defect-B-H2	H2	X	O_3	O_3	O_6	Al_6	O_6	O_3	O_3	O_6	Al_{12}	*R*

ii. Hydrated Ideal Surfaces

Figure 4. Side views of the optimized Hydrated Ideal surfaces. Dotted/dashed gold lines correspond to singly-coordinated oxygen functional group layers (AlO); flat, straight orange lines correspond to doubly-coordinated oxygen functional group layers (Al_2O); dashed red lines correspond to triply-coordinated oxygen functional group layers (Al_3O); dotted blue and maroon lines correspond to aluminum and bulk oxygen layers, respectively.

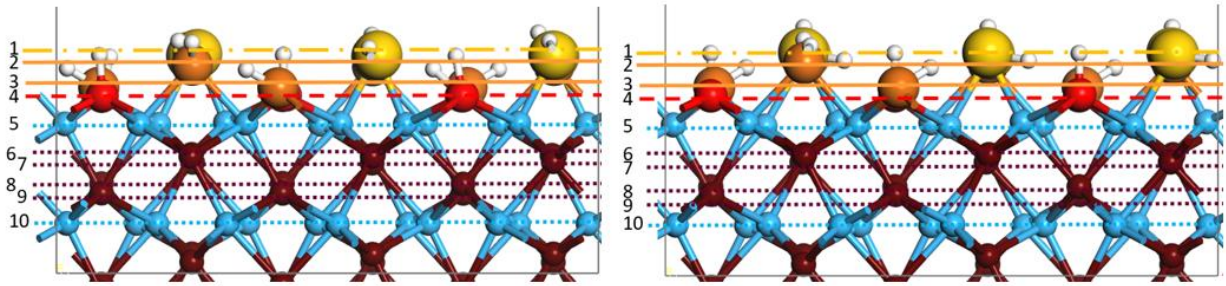

In order to model possible hydrated surfaces, under-coordinated oxygen functional groups are capped with hydrogen, following the approached take in previous work on the (012) surface.[28] The resulting optimized Perfect-H1 and Perfect-H2 models are illustrated in Figure 4, which correspond to the defect-free, unreconstructed surface sample obtained by low temperature annealing. The layering sequence for Perfect-H1 is H_1-O_6-O_3-O_3-O_6-Al_{12}-*R*. Two H orientations were initialized for the H2 hydration scheme to explore hydrogen bonding networks. In one, the aquo groups are in-plane with the aluminum atoms and in the second they are out of plane relative to the surface. Both structures lead to the same geometry with a tilted hydrogen structure, so only one Perfect-H2 result is reported. Furthermore, in the optimized geometry, Perfect-H2 exhibits mixed protonation of AlO and Al_3O groups. This is a result of one half of the singly-coordinated aquo groups in the initial structure donating one hydrogen atom to one half of the neighboring triply-coordinated oxygen; alternatively, all of the doubly-coordinated Al_2O groups remain singly-protonated. The optimized Perfect-H2 surface contains singly-coordinated aquo groups, singly-coordinated hydroxyl groups, two different doubly-coordinated hydroxyl groups, triply-coordinated hydroxyl groups, and triply-coordinated oxo groups. The layer sequencing for this structure is therefore H_2-O_6-O_3-O_3-O_6-Al_{12}-*R*.

iii. *Hydrated Defect Surfaces*

Based on the stoichiometry of the high temperature annealed sample from the experimental study, four different hydrated Defect structures are modeled: Defect-A-H_1, Defect-A-H2, Defect-B-H1, and Defect-B-H2. The H1/H2 termination is the same as described previously. Side views of these structures are shown in Figure 5. To maintain charge-balanced slabs, the hydrated surfaces have additional layers of O as compared to their O-terminated counterparts. The stacking sequence for Defect-A-H1/H2 and Defect-B-H1/H2 can then be presented as: H1/H2-O_6-X_3-X_3-O_6-Al_6-O_6-O_3-O_3-O_6-Al_{12}-R and H_1/H_2-X_6-O_3-O_3-O_6-Al_6-O_6-O_3-O_3-O_6-Al_{12}-R, respectively.

Figure 5. Side views of the optimized Hydrated Defect surfaces. Dotted/dashed gold lines correspond to singly-coordinated oxygen functional group layers (AlO); flat, straight orange lines correspond to doubly-coordinated oxygen functional group layers (Al_2O); dashed red lines correspond to triply-coordinated oxygen functional group layers (Al_3O); dotted blue and maroon lines correspond to aluminum and bulk oxygen layers, respectively. The layer sequencing for a given defect type (A or B) is same regardless of the hydrogen termination type, and the lowest exposed oxygen layer for both defect types is L8.

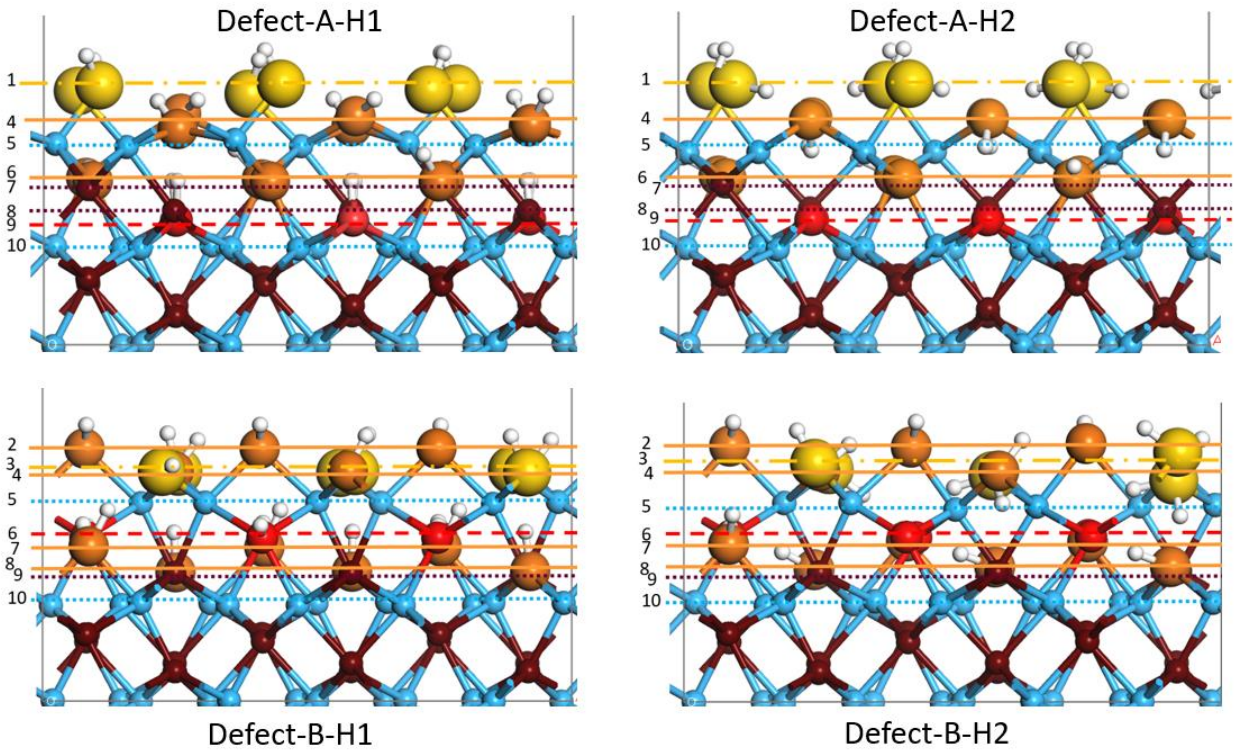

3. Results & Discussion

3.1. Layer Spacing

We analyze DFT-relaxed structures for the nine models, reporting the spacing between consecutive layers. We also present the percentage deviation relative to bulk spacings. This information can be found in in Tables 2-5.

i. Oxygen-Terminated Structures

As reported in Table 2, in the Perfect-O model, terminal layers L3-L4 show an outward relaxation of 30% with respect to the bulk. In layer L4-L5, the relaxation is inwards by 7% relative to the bulk. Terminal layers have a 'non-ideal' coordination environment as compared to the bulk and are therefore prone to undergo such relaxations.

As noted earlier, the experimental study on the (110) surface supports that the defect sample, prepared at the higher annealing temperature, is suggested to have Type A dimer groups missing from the surface. Surface relaxations of models with different dimer groups removed can assist in confirming the experimental structure. While Al atoms belonging to dimer A relax inwards by 0.04 Å, Al atoms belonging to dimer B relax outwards by 0.07 Å. The spacing between layers L4-L5 is reduced from 0.69 Å (-7%) in Perfect-O to 0.51 Å (-31%) in Defect-A-O. The significant inwards relaxation is expected for the Defect-A-O. This is because removing a full diagonal layer from the termination reduces the surface Al coordination numbers to three as half of the Al atoms (six) are removed from the layer. In the case of the Defect-B-O structure, the bulk value for layer L4-L5 spacing is 0.94 Å. However, in the relaxed

structure this value reduces to 0.88 Å. This 6% inward relaxation is accompanied by a noticeable inwards relaxation in layers L5-L6 separation (37%). The 37% inwards relaxation in layers L5-L6 of Defect-B-O is significantly larger than its counterpart in Perfect-O (16%). This is also expected as the vertical relaxation in a defect structure ought to be larger than its perfect counterpart so as to recover the bulk-like bonding character. Vertical relaxations of outermost Al dimers are also different in Defect-A-O and Defect-B-O. While in the former the Al atoms belonging to dimer B relax outwards by 0.32 Å, in the latter, the Al atoms belonging to dimer A relax inwards by 0.11 Å. These relaxations, while in the same direction as those of a Perfect-O structure, are of greater magnitude in a Defect structure. Another indication of the larger relaxation in the Defect structure as compared to the Perfect one can be found in the case of O_3-O_3 spacing in Perfect-O as compared to the same spacing in Defect-A-O. In this case the former separation is 35% outwards and the latter is 43% outwards. The same is true for O_6-O_3 in Perfect-O vs. Defect-B-O (10% vs. 15% outwards). Full details are presented in Table 2.

Table 2. Calculated layer spacings (Å) and percent relaxations with respect to theoretical bulk spacing (%Δ) for Oxygen-Terminated structures.

Layers	Perfect-O	Spacing (Å)	%Δ	Defect-A-O	Spacing (Å)	%Δ	Defect-B-O	Spacing (Å)	%Δ
L3-L4	O_3-O_6	0.26	+30	-	-	-	-	-	-
L4-L5	O_6-Al_{12}	0.69	-7	O_6-Al_6	0.51	-31	O_3-Al_6	0.88	-6
L5-L6	Al_{12}-O_6	0.62	-16	Al_6-O_3	1.00	+6	Al_6-O_6	0.47	-37
L6-L7	O_6-O_3	0.22	+10	O_3-O_3	0.77	+43	-	-	-
L7-L8	O_3-O_3	0.73	+35	O_3-O_6	0.32	+60	O_6-O_3	0.85	+15
L8-L9	O_3-O_6	0.13	-35	O_6-Al_6	0.51	-31	O_3-O_6	0.28	+40
L9-L10	O_6-Al_{12}	0.70	-5	Al_6-Al_6	0.21	-	O_6-Al_{12}	0.67	-10

ii. *Hydrated Ideal Structures*

As shown in Tables 1 and 2, the Perfect-H structures have two additional O layers as compared to Perfect-O structures. In order to achieve charge balance in the Perfect-H structures, 18 H atoms are added to each face of the slab. As the Perfect-H models are representative of the structural fit for the low-temperature annealed sample from the experimental study, the experimental data can be used for comparison. As shown in Table 3, overall, the layer spacing of both Perfect-H structures are in good agreement with the experimental data. Comparisons of the Hydrated Ideal layer and Oxygen Terminated surfaces details how hydration effects influence surface relaxations. For example, the O_3-O_6 separation in Perfect-O is +30% (0.26 Å) whereas the same value is +20% (0.20 Å) and +15% (0.18 Å) for Perfect-H_1 and Perfect-H_2, respectively. This is due to two reasons: The presence of two additional O layers in the Perfect-H structures reduces the amount of vertical relaxation as compared to Perfect-O. Secondly, the presence of H atoms helps recover the bonding on the surface O atoms, resulting in less relaxation of inner-layer O atoms.

The hydration scheme (H1 or H2) has a measurable effect on the interlayer spacings. The largest difference between spacings for the two hydration schemes is 0.08 Å occurring in the case of layers L7-L8 (O_3-O_3). The topmost Al atoms that belong with different dimer types undergo relaxations in opposite directions. This is in line with what was observed for the Oxygen-Terminated structures. However, the magnitude and direction of relaxations for Perfect-H are different than for Perfect-O. While Al atoms from dimers of Type A experience an average outwards relaxation of 0.07 Å, Al atoms from dimers of Type B experience an average inwards relaxation of 0.12 Å. Comparing the surface relaxations in Perfect-O and Perfect-H structures demonstrates the effect of hydration on the extent and type of optimized atomic layer spacing values. As Perfect-H1 and Perfect-H2 have an equal number of surface protons, the reported surface relaxation are mostly comparable.

iii. *Hydrated Defect Structures*

Layer spacings for Hydrated Defect models A-H1/2 are presented in Table 4. Also included in Table 4 are the layer spacings for the best fit structural model for the high-temperature annealed sample from the experimental study, which is the basis for the design of Defect A structures. Compared to the bulk, both Defect-A-H1 and H2 exhibit greater relaxation in layer spacing than either of the Hydrated Ideal structures. While the hydration scheme had minimal impact on the layer spacings in the Perfect-H structures, and agreed well with the best fit model for the low-temperature annealed experimental sample, here for the Hydrated Defect models we note significant structural differences as a function of hydration scheme. While the absolute value of deviation from the experimental data in layers L4-L5 and L5-L6 of the Defect-A-H1 is ~50%, this value for Defect-A-H2 is only -21% for the layers L4-L5 and 0% for layers 5-6. Overall, H2 hydration scheme reproduces the experimentally-observed spacing values better than the H1 scheme. In the case of Defect-B-H structures, Table 5, no experimental structural data is available for comparison. The effect of hydration scheme on the spacings in this case is again inconsequential. The largest deviation of a spacing value with respect to the bulk takes place at layers L3-L4. Plus, Al atoms of dimer A in Defect-B-H1 undergo an inwards relaxation of 0.11 Å, whereas Al atoms of dimer B in Defect-A-H1 undergo an inwards displacement of 0.16 Å. Substantial lateral relaxation of surface Al atoms is observed in the case of Defect-B-H too. For example, Al atoms of dimer A in Defect-B-H1 undergo lateral relaxations of -2.1% and -2.0% along *a* and *b* axes, respectively. Also, lateral effects are measured as -6.3% along *a* axis in the case of Defect-B-H2. This effect has potential implications. Given that surface atom displacements are driven by the need to recover the bonding character of the atoms, a larger in-plane displacement is an indication of a more destabilized surface structure. As such, the greater displacement of surface atoms in Defect-B-H2 is indicative of possible less stability of this surface compared to Defect-B-H1. However, a more scientifically recognized metric is required to assort the relative stabilities of all the surface terminations characterized herein.

Table 3. Calculated layer spacings (Å) and percent relaxations with respect to theoretical bulk spacing (%Δ) for the Hydrated Ideal structure class. Experimental data is for the defect-free model and is in Ref. 10.

Layers		Perfect-H**1**	$\%\Delta_1$	Perfect-H**2**	$\%\Delta_2$	Expt.	$\%\Delta_{H1}$	$\%\Delta_{H2}$
L1-L2	O_6-O_3	0.24	+20	0.23	+15	0.19	-18	+21
L2-L3	O_3-O_3	0.54	0	0.58	+7	0.56	-4	+4

L3-L4	O_3-O_6	0.20	+5	0.18	-5	0.19	+5	-5
L4-L5	O_6-Al_{12}	0.67	-8	0.69	-6	0.92	-27	-25
L5-L6	Al_{12}-O_6	0.77	+6	0.75	+3	0.77	0	-3
L6-L7	O_6-O_3	0.17	-15	0.16	-20	0.19	-11	-16
L7-L8	O_3-O_3	0.51	-6	0.59	+9	0.69	-26	-15
L8-L9	O_3-O_6	0.23	-21	0.18	-5	0.19	+21	-5
L9-L10	O_6-Al_{12}	0.74	+1	0.74	+1	0.58	+28	+28

Table 4. Calculated layer spacings (Å) and percent relaxations with respect to theoretical bulk spacing (%Δ) for Hydrated Defect-A structure class. Experimental data is for the defect model from Ref.[41]

Layers		Defect-A-H**1**	$\%\Delta_1$	Defect-A-H**2**	$\%\Delta_2$	Expt.	$\%\Delta_{H1}$	$\%\Delta_{H2}$
L4-L5	O_6-Al_6	0.54	-26	0.79	+8	1.00	-46	-21
L5-L6	Al_6-O_6	0.90	+23	0.61	-16	0.61	+48	0
L6-L7	O_6-O_3	0.19	0	0.18	-5	0.19	0	-5
L7-L8	O_3-O_3	0.55	+2	0.62	+14	0.77	-29	-20
L8-L9	O_3-O_6	0.24	+20	0.27	+35	0.19	+26	+42
L9-L10	O_6-Al_{12}	0.68	-7	0.70	-4	0.74	-8	-5

Table 5. Calculated layer spacings (Å) and percent relaxations with respect to theoretical bulk spacing (%Δ) for Hydrated Defect-B (hypothetical defect surface). Experimental data is for this model is unavailable.

Layers		Defect-B-H**1**	$\%\Delta_1$	Defect-B-H**2**	$\%\Delta_2$
1-2	O_6-O_3	-	-	-	-
2-3	O_3-O_3	0.55	+2	0.59	+9
3-4	O_3-O_6	0.02	-90	0.04	-79
4-5	O_6-Al_6	0.77	+6	0.87	+19

5-6	Al_6-O_6	0.86	+18	0.76	+4
6-7	O_6-O_3	0.23	+21	0.15	-21
7-8	O_3-O_3	0.62	+15	0.62	+14
8-9	O_3-O_6	0.03	-85	0.10	-50
9-10	O_6-Al_{12}	0.78	+7	0.76	+4

3.2. Bond Valence Results

As noted in the Introduction, the principles of bond-valence offer a means for understanding structure-reactivity relationships in mineral-water interfaces. In the empirical BV model, bond strengths are inversely related to bond lengths within the following formula:[16, 32-34, 48-49, 59]

$$s_i = \exp\left(\frac{R_{ij}^0 - R_{ij}}{b}\right) \quad (5)$$

where s_i is the bond valence term in valence units (v.u.), R_{ij} is the observed cation-oxygen bond length, and R_{ij}^0 is a tabulated parameter corresponding to the ideal bond length. The parameter *b* is an empirical constant with a value of 0.37 Å. Brese and O'Keeffe have tabulated parameters R_{ij}^0 and *b* for cations bound to oxygen, with values of 1.651 Å and 0.95 Å for O-Al and O-H bonds, respectively.[48] Hydrogen bonding effects on bond valence sums are accounted using the form developed by Bargar et al. and using a distance threshold of 2.5 Å.[34] The surface oxygen bond valence sum (BVS) for a given atom is calculated by summing all of the s_i values for a given oxygen atom:

$$BVS = \sum s_i \quad (6)$$

The model parameters are fit, using known bulk structures, such that the BVS value equals the absolute value of the oxidation state of the ion. When applied to surfaces, it is assumed that exposed oxygen groups with BVS values close to the ideal value are the most stable, and relatively non-reactive towards sorption. In other words, the BVS indicates the degree of coordination saturation for oxygen functional groups, implying whether or not these groups are likely to react (through (de)protonation or sorption) to obtain the ideal bonding requirements.

While there is no rigorous way to relate bond valence to bond energies, the correspondence between stability and structure has motivated the development of potentials based on BV principles in materials spanning binary and ternary oxides, main-group and transition metals, and nanocomposites. In other work, DFT calculations of Pb(Zr,Ti)O_3 solid solutions were used to fit BV-based potentials, which went on to be used in larger-scale simulations. Based on the indications of a link between energy and bond valence, we compute the BVS values for the DFT geometry-optimized (110) surface structures studied here. We go on in later sections to then compare the inferred stability, based on the BVS values, to electronic structure analysis of the surface functional group. The resulting BVS values are reported in Tables 6-9.

i. Oxygen-Terminated

Table 6. Bond Valence Sums (BVS) in v.u. for exposed oxygen layers in the clean, oxygen-terminated surfaces.

(012) α-Al_2O_3		Perfect-O		Defect-A-O		Defect-B-O	
Al_3O (L1)	1.74	Al_2O (L3)	1.59	Al_2O (L4)	1.00	Al_2O (L4)	1.14
Al_4O (L3)	1.80	Al_3O (L4)	1.71	Al_2O (L8)	1.70	Al_2O (L7)	1.28
				Al_3O (L9)	1.51	Al_3O (L6)	1.50

We begin by comparing the BVS for the (110) Perfect-O to the oxygen-terminated A1-cut of the (012) α-Al_2O_3, previously studied by Mason et al .[58] For the top two layers of oxygen, the BVS values are higher in (012) compared to (110) Perfect-O, which indicates relative stability of the (012) surface.

Of the (110) oxygen-terminated surfaces, Perfect-O surface has the largest BVS for the different layers of oxygen that are exposed. This is the defect-free surface, where there is one layer of doubly-coordinated (Al_2O L3) and one layer of triply-coordinated (Al_3O L4) oxygen atoms exposed. The BVS for Al_2O L3 is lower than that of Al_3O L4, which is due to the lesser coordination; a greater amount of bonds and/or the shorter those bonds are corresponds to a larger BVS.

In both Defect-A-O and Defect-B-O, the defects result in additional oxygen exposure of lower layer atoms. The Al_2O L4 is lower in Defect-A-O than Defect-B-O by 0.14 v.u., which is due to the missing triply-coordinated layer L6. Because L6 is absent in Defect-A-O, the O in L8 are exposed and become triply-coordinated.

ii. Hydrated Ideal

Table 7. BVS in v.u. for exposed oxygen layers in the Hydrated Ideal Perfect surfaces with H1 and H2 termination types.

Perfect-H1		Perfect-H2	
AlOH (L1) (A)	1.97	$AlOH_2$ (L1)	2.01
AlOH (L1) (B)	1.85	AlOH (L1)	1.97
Al_2OH (L2)	2.04	Al_2OH (L2)	2.01
Al_2OH (L3)	2.20	Al_2OH (L3)	2.20
Al_3OH (L4)	2.01	Al_3OH (L4)	2.01
		Al_3O (L4)	1.80
Average	2.01	Average	2.00

In the Perfect-H1 structure, there are two different singly coordinated oxygen functional groups with distinct BVS values, labeled A/B. Additionally, both termination types have Al_2O BVS that exceed the ideal value of 2. The average BVS of Perfect-H1 and Perfect-H2 are very similar, differing by only 0.01 v.u.

iii. Hydrated Defect

a. Defect-A

Table 8. BVS for exposed oxygen layers in the Defect-A surfaces with H1 and H2 termination types.

Defect-A-H1		Defect-A-H2	
AlOH (L1)	1.76	AlOH (L1)	1.86

Al_2OH (L4)	1.90	Al_2OH (L4)	1.74
Al_2OH (L6)	2.08	Al_2OH (L6)	2.18
Al_3OH (L9)	2.01	Al_3OH (L9)	1.96
Average	1.94	Average	1.93

Comparing the average BVS for the two hydrogen terminations, the averages are very similar, only differing by 0.01 v.u. This is expected since the two hydrogen terminations relax to very similar structures, with differences largely being hydrogen orientation.

b. Defect-B

Table 9. BVS for exposed oxygen layers in the Defect-B surfaces with H1 and H2 termination types.

Defect-B-H1		**Defect-B-H2**	
Al_2OH (L2)	1.90	Al_2OH (L2)	1.88
AlOH (L3)	1.82	$AlOH_2$ (L3)	1.89
Al_2OH (L4)	1.99	Al_2OH (L4)	1.89
Al_3OH (L6)	1.99	Al_3O (L6)	1.93
Al_2OH (L7)	2.08	Al_2OH (L7)	2.03
Al_2OH (L8)	2.18	Al_2OH (L8)	2.16
Average	1.99	Average	1.96

In both hydrogen terminations, increasing the layer depth, increases the BVS for oxygen atoms. The singly-coordinated AlO in L3 has only one hydrogen atom in H1, and having two hydrogen atoms in H2 causes an increase in the BVS of 0.06 v.u. Additionally, the triply-coordinated Al_3O in L6 have one proton in H1, and the BVS decreases in H2 by 0.06 v.u. because these oxygen atoms have no protons. In H1 and H2, both of the doubly-coordinated Al_2O in L7 and L8 have BVS that exceed the ideal value of 2; this indicates that these oxygen atoms are oversaturated in terms of bonding. The larger BVS is likely due to the fact that these oxygen atoms are deeper in the surface and are able to retain bulk-like character. Comparing overall average BVS for the two hydrogen terminations, Defect-B-H1 has an average BVS that is 0.03 v.u. greater than Defect-B-H2 and is closer to the ideal oxygen BVS value of 2 v.u., indicating better coordination saturation for the exposed oxygen atoms. The difference in average BVS values indicates that the preferred hydrogen terminations for this defect to be Defect-B-H1.

Comparing the BV results for the Hydrated Ideal and Hydrated Defect surfaces, the results are similar, regardless of the hydration scheme. The average BVS for the Perfect-H structures are the closest to ideal of 2 v.u.; the most significant deviation is found in the hydrated Defect-A surface, differing by at most 0.07 v.u. For the six hydrated surfaces, the average BVS differs by at most 0.08 v.u. These results imply that these surface functional groups exhibit similar coordination and reactivity and that the two different hydration schemes have similar effects on surface stability. The tabulated BVS values show cases in which the oxygen functional group coordination and/or protonation state differ, yet result in nearly identical results. For example, Perfect-H2 has three identical BVS values of 2.01 v.u. for oxygen functional groups for which the surface coordination number varies between 1 and 3 (AlO, Al_2O, and Al_3O).

3.3. Surface-Free Energies at 0 K

Figure 6. Free energies of model surface terminations for α-Al_2O_3, as determined by ab initio thermodynamics. Surface structures are detailed in the text.

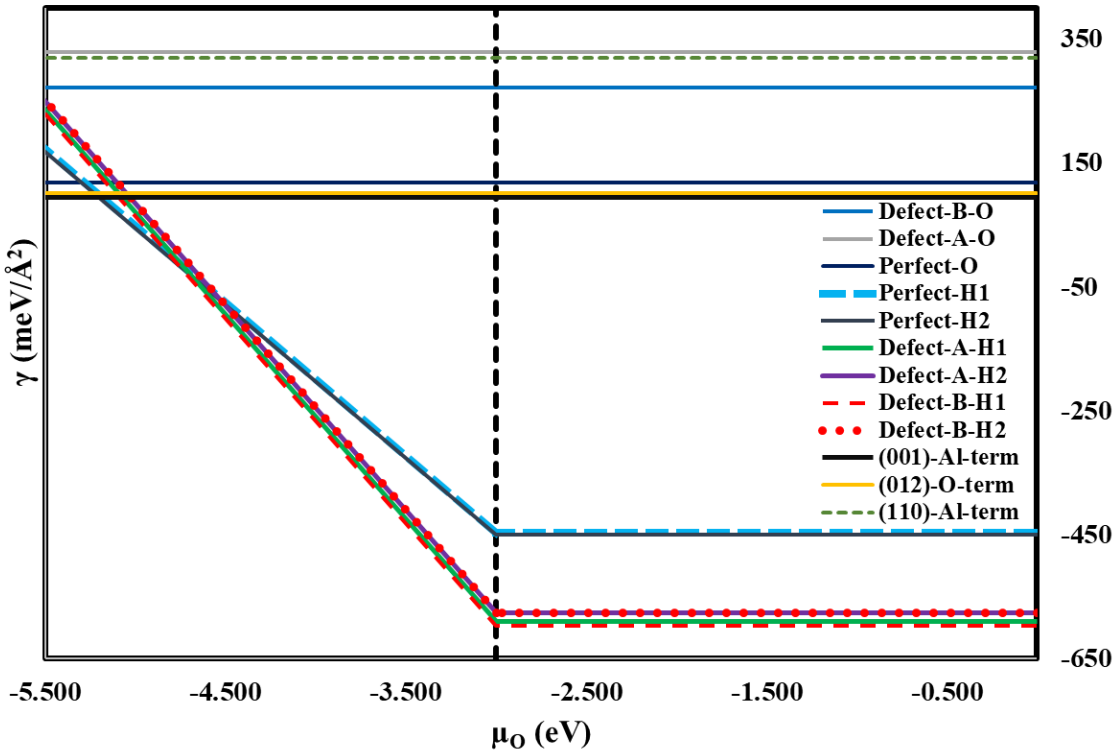

The ab initio thermodynamics-calculated surface-free energies offer insights into the relative stabilities of the surface models under variable conditions, as reflected by μ_O. Figure 6 shows surface-free energy values calculated at 0 K, using Eq. (3).

First, we compare the values of γ for the (110) Perfect O model to the Al-terminated (001) surface and the stoichiometric (012) surface, where the latter two are the known preferred structures under oxygen poor conditions. The values of γ for the (110) Perfect O, (012), and (001) models are 117.8, 100.5, and 94.4 meV/Å^2, respectively. The relative values for (012) and (001) are in good agreement with previous reports using different DFT implementations.[28, 38] Collectively, the results confirm that the (001) surface is the most stable, followed by (012) and (110), respectively. While the experiments were done in situ, we briefly explore the (110) surface structure under oxygen poor conditions by comparing oxygen-terminated (Perfect O) and aluminum-terminated ((110)-Al-term) structures that are both charge-neutral. As shown in Figure 6, the associated values of γ are 117.8 and 319.8 meV/Å^2, respectively. Owing to the relatively high value of γ for the (110)-Al-term structure, we do not include it in further discussion of results.

Figure 6 can also be used to assess how hydration affects surface stability. Starting on the left-hand side at low values of μ_O, the most favorable (110) surface structure is the Perfect-O model. However, as μ_O increases, the hydrogen terminated models become more favorable. The discontinuity at μ_O=-3.00 eV corresponds to the crossover from when the hydrogen chemical potential is determined through equilibrium with H_2 (to the left) or H_2O (to the right). At the far right of the plot, the most stable surfaces are the hydrated forms. The Hydrated Ideal surfaces have values of γ in the range of -450.7 to -447.2 meV/Å^2, while the range for the Hydrated Defect surfaces is -596.6 to -575.6 meV/Å^2. This demonstrates

that kinetically trapped surfaces can, after hydration is introduced, result in hydrated surfaces that are more stable than their ideal counterparts.

The values of γ also show that there are many nearly degenerate structures in the Hydrated Defect class. For instance, the energy difference between Defect-A-H1 and Defect-B-H1 is only 6.30 meV/Å^2, which is essentially degenerate within the accuracy of the calculations. This difference is smaller than thermal energy at room temperature (k_BT~26 meV). For example, the value of γ for Defect-A-H1 is not appreciably different than that of Defect-A-H2 (~14 meV/Å^2). This can be interpreted by the fact that hydrogen can satisfy undercoordinated bonding environments. As shown in Table 8, the Defect-A-H1/H2 structures both exhibit satisfied oxygen bonding environments as reflected through the average oxygen bond valances sum values of 1.94 and 1.93 v.u. This is similar to how the bond valence sums in Table 9 for Defect-B-H1/H2 have satisfied values of 1.99 and 1/.96 v.u., respectively. In preliminary work, we studied structures that exhibited different ratios of removed Type A:B dimer groups. However, upon hydration, the results were degenerate within 10-15 meV/Å^2, and therefore we only report the defect structures in which all Type A/Type B dimer groups are removed.

3.4. Thermodynamic stability at finite *T*

To further relate the surface modeling to realistic conditions, we go on to calculate values of γ of the surfaces under two different sets of conditions. For the first set of conditions, γ is calculated at $p_{H_2O} = p_{O_2} = 10^{-8}$ kPa, corresponding to UHV conditions. The second set of conditions uses $p_{O_2} = 20$ kPa, and p_{H_2O} is 3.2 kPa, the saturated vapor pressure at 298.15 K and corresponding to "wet" conditions. As discussed in the Methodology and Computational Details section, temperature effects of the slab stability are taken into account by calculating the vibrational contribution to the Gibbs free energy.

i. UHV Conditions

Only the Oxygen Terminated surfaces are germane to the discussion of results under UHV conditions. As reported in Table 10, Perfect-O is the most stable O-terminated surface at 0 K. This is consistent with our γ vs. *T* diagram at 0 K. On the other hand, Defect-B-O is more stable than Defect-A-O, by 57.6 meV/Å^2. For all the O-terminated surfaces, the free energy declines as the temperature increases. This is because chemical potential decreases with increasing the temperature. We note that over the temperature range of 0-600 K, there are no crossovers between values of γ for the Perfect-O, Defect-A-O, or Defect-B-O structures. As all the O-terminated surfaces are stoichiometric, the surface-free energy is independent of the O chemical potential. However, the temperature dependence is mainly driven by enthalpy and entropy effects that are factored in the chemical potential of the alumina, $\mu_{Al_2O_3}$, and vibrational effects. It should be underscored that the effect of vibrational motions is non-negligible for both O-terminated and H-terminated α-Al_2O_3 surfaces.

Table 10. Surface-free energies of O-terminated structures at 10^{-8} *kPa* various temperatures (meV/Å^2).

	0 K	298.15 K	600 K
Perfect-O	117.8	115.4	110.7
Defect-A-O	328.9	324.8	317.1
Defect-B-O	271.3	268.4	262.8

ii. Ambient Conditions

Figure 7. Surface-free energy vs. temperature for H-terminated structures.

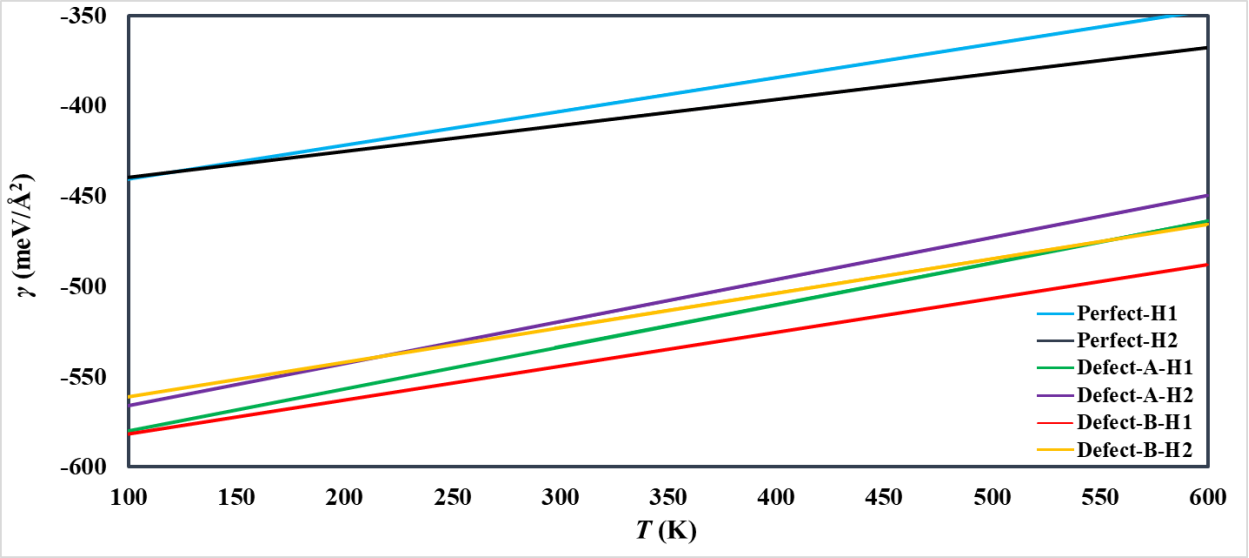

By calculating the values of γ for the hydrated surfaces over a temperature range of 0-600 K (Figure 7), we can assess whether interconversion between the Hydrated Ideal and Hydrated Defect categories is favorable. While there are crossovers in values of γ within a class, there are no crossovers between the Hydrated Ideal and Hydrated Defect classes. At 600 K, the difference between the classes is still at least 82 meV/Å^2. This suggests that once a surface is kinetically trapped into either class, it maintains its overall stoichiometry, but can undergo favorable hydrogen rearrangement.

a. Hydrated Ideal

A crossover point was found between Perfect-H1 and Perfect-H2 surfaces at 126.44 K. the difference between the energetics of these two terminations continues to increase at temperatures beyond the crossover point. However, this difference remains small at room temperature of 298.15 K (7.47 meV/Å^2). This indicates that both schemes provide similar stabilization through hydrogen bonding.

b. Hydrated Defect

As shown in Figure 7, there are multiple crossovers between Hydrated Defect structures over the investigated temperature range. However, the similar values of γ for Defect-A-H2, Defect-B-H2, Defect-A-H1 and Defect-B-H1 show competing thermodynamic stability, suggesting that defects formed through removal of different dimer types are nearly degenerate in hydrated form. Because of the degeneracy in the surface-free energy values for the Hydrated Defect surfaces, it is difficult to discern which type of dimer is missing in

the reconstructed surface. The Hydrated Defect surfaces may exist in equilibrium with each other under ambient conditions.

In comparing the surface-free energy results to the experimental characterization[41], the results are consistent in that both Hydrated Ideal and Hydrated Defect models are predicted to be stable. While the Hydrated Defect models exhibit lower values of γ relative to the Hydrated Ideal class, it is likely the case the surface preparation conditions would trap the sample into one of the two classes. As shown in Figure 7, there are no crossovers between classes, which further supports that two distinct structural classes could persist based on sample history. Finally, the many nearly-degenerate Hydrated Defect structures suggest that while a single best fit structure was proposed for the high-temperature annealed sample, other related structures could occur.

3.5. Electronic Structure Calculations

Projected density of states (PDOS) is an analysis that provides a chemically intuitive description of electronic structure.[60] As discussed in the Introduction, geochemical surface science is often discussed in the context of BV structure-reactivity relationships, in which the coordination of oxygen to surface aluminum, along with the protonation state, are key factors. Here, we aim to further characterize distinct oxygen functional groups through electronic analysis. For this reason, we study the Perfect-H2 surface, as it exhibits six unique function groups. Specifically, the surface contains one singly-coordinated aquo group, one singly-coordinated hydroxyl group, two doubly-coordinated hydroxyl groups (of varying depth in the surface), one triply-coordinated hydroxyl group, and one triply-coordinated oxo group, as shown in Figure 8.

Figure 8. Top view of surface Perfect-H2 atoms and their coordination environments, where red indicates a singly-coordinated aquo group, blue indicates a singly-coordinated hydroxyl group, green indicates a doubly-coordinated hydroxyl group in L2, purple indicates doubly-coordinated hydroxyl group in L3, gold indicates a triply-coordinated hydroxyl group, and orange indicates a triply-coordinated oxo group.

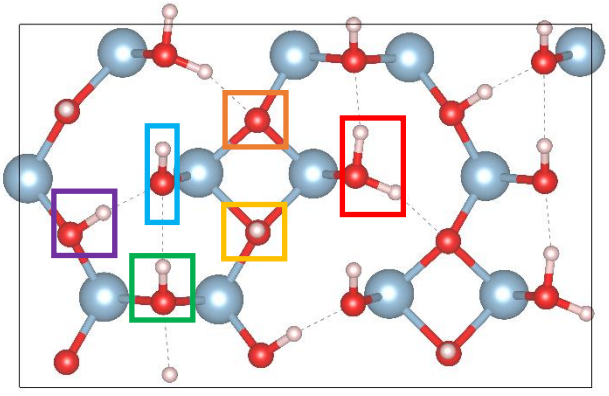

Figure 9. PDOS plot for Perfect-H2 topmost O atoms, where the color scheme corresponds to the functional groups identified in Figure 8. In all cases, the Fermi level is referenced to 0 eV. The BVS from Table 7 have been included

above each PDOS, in units of v.u.

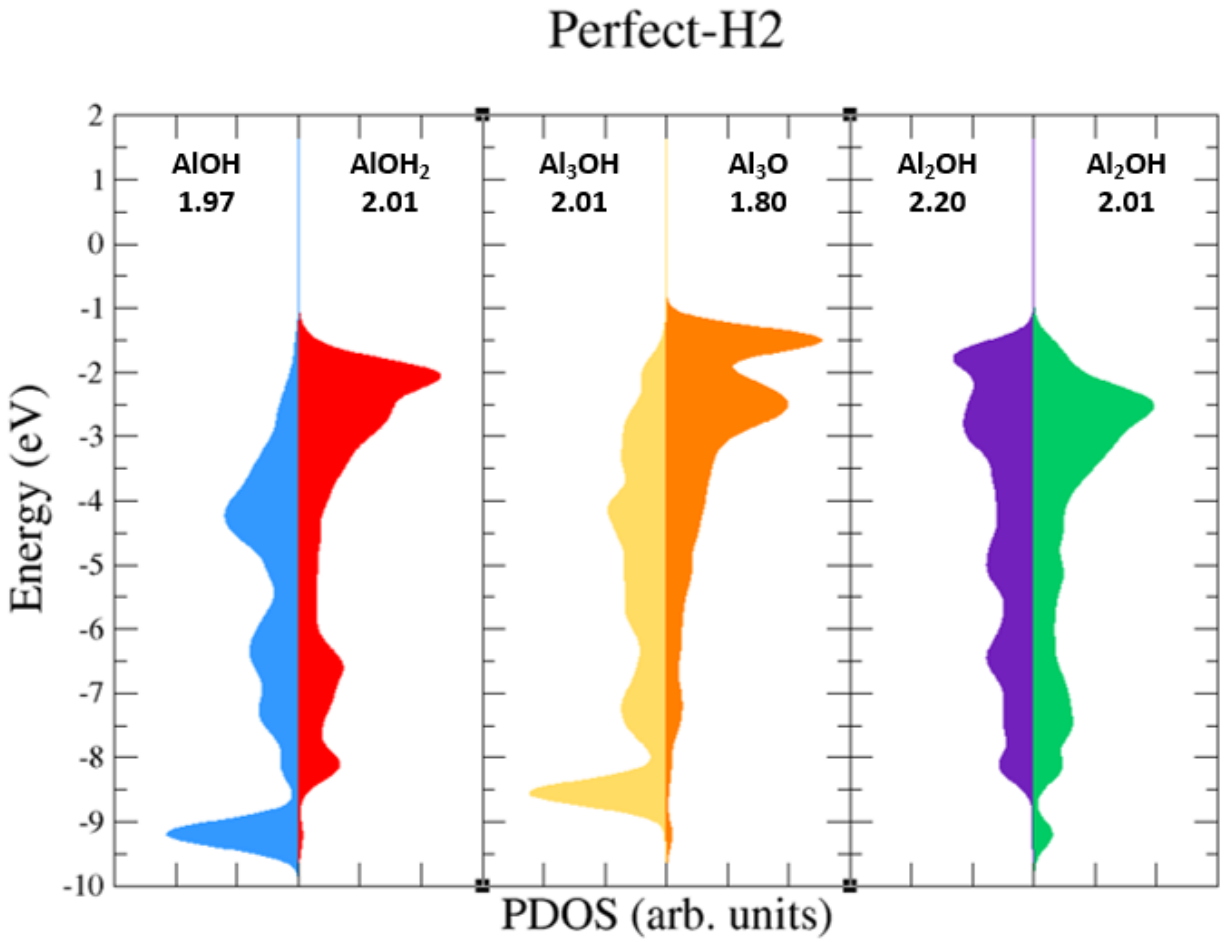

As all the p-states are completely filled for ionized O atoms in Al_2O_3, no empty states were observed for these atoms in the PDOS presented in Figure 9. The electronic structure should be a better indicator of functional group reactivity than BVS values, which are based on an empirical bulk model. For instance, the BVS values for $AlOH_2$ (L1) and Al_3OH (L4) are 2.01 v.u. However, their PDOS plots are qualitatively different (red vs. gold). Specifically, the PDOS for $AlOH_2$ (L1, red) exhibit more density near the Fermi level, an indicator of high surface reactivity. There are cases in which BVS predictions and PDOS are in better agreement. As the PDOS in Figure 9 indicates, the Al_3O (L4, orange) is the most reactive surface oxygen functional group, corresponding to the lowest BVS in Table 7 of 1.80 v.u. The PDOS shows most of the electron density near the Fermi level, indicative of a reactive surface site. The PDOS suggests different reactivity for the two doubly-coordinated hydroxyl groups, reflected by their different BVS: 2.01 (green) and 2.20 (purple). Bond-valence alone is unable to differentiate three of the oxygen functional groups, having identical values of 2.01 v.u. for the singly-coordinated aquo (red), doubly-coordinated hydroxyl (green), and triply-coordinated hydroxyl (yellow). Figure 9 shows differences in the PDOS, indicating different reactivity for these three functional groups.

Surface atoms have a more flexible bonding environment compared to bulk atoms. As such, surface relaxations can recover coordination in ways that the bulk BV model would not capture. For example, the BVS for Al_2OH (L3) indicates overcoordination, and Al_3O (L4) indicates undercoordination. If a

hydrogen atom is transferred between these groups in an attempt to balance the coordination and bring the BVS to the ideal value of 2 v.u., the Al_2OH (L3) will recover the proton over the course of geometry optimization. The resulting structure resembles that of Perfect-H1, and is energetically degenerate. This shows that by attempting to satisfy BV requirements, the resulting structure is not the most stable one.

As surface-adsorbate interactions depend on both overlap and energy matching, electronic structure descriptions provide insights into reactivity that go beyond bulk-parametrized BV analysis. This has been shown, for example, in terms of directional bonding of Pb^{2+} on the (012) surface[24, 35, 58, 61]and the effects of adsorption-induced strain in oxyanion complexes[49, 62-63].

Conclusions

DFT and atomistic thermodynamics modeling of the α-Al_2O_3 (110)-water interface support experimental studies that report two structures depending on preparation conditions. Specifically, the calculations show that both hydrated ideal and hydrated defect structures are stable and do not interconvert, suggesting that samples may be kinetically trapped into either group. The calculated surface-free energy of hydrated defect surfaces is found to be lower than that of ideal terminations, which supports that metastable surfaces can be stabilized when exposed to water, and that surface preparation conditions can dictate mineral-water interface structure. The Perfect-H2 structure, which is based on the best-fit structure for the experimental low-temperature annealed sample, is found to have the lowest surface-free energy of the hydrated, defect-free models. Also, while the protonation state cannot be determined experimentally, the good structural agreement in terms of interlayer spacing suggests that the Perfect-H2 model is a reasonable representation of the hydrated α-Al_2O_3 (110) surface. As this structure exhibits a broad range of oxygen functional groups (in terms of coordination to Al and protonation state), this provides a useful model for future studies of ion sorption that probe mineral-water interface structure-reactivity.

References

1. Brown, G. E., et al., Metal Oxide Surfaces and Their Interactions with Aqueous Solutions and Microbial Organisms. *Chemical Reviews* **1999**, *99*, 77-174.
2. Al-Abadleh, H. A.; Grassian, V. H., Oxide Surfaces as Environmental Interfaces. *Surface Science Reports* **2003**, *52*, 63-161.
3. Kelemen, P. B.; Matter, J., In Situ Carbonation of Peridotite for CO_2. Storage. *Proceedings of the National Academy of Sciences* **2008**, *105*, 17295.
4. Oelkers, E. H.; Gislason, S. R.; Matter, J., Mineral Carbonation of CO_2. *Elements* **2008**, *4*, 333-337.
5. Kappler, A.; Straub, K. L., Geomicrobiological Cycling of Iron. *Reviews in Mineralogy and Geochemistry* **2005**, *59*, 85-108.
6. Brown, G. E.; Parks, G. A., Sorption of Trace Elements on Mineral Surfaces: Modern Perspectives from Spectroscopic Studies, and Comments on Sorption in the Marine Environment. *International Geology Review* **2001**, *43*, 963-1073.
7. Luthy, R. G.; Aiken, G. R.; Brusseau, M. L.; Cunningham, S. D.; Gschwend, P. M.; Pignatello, J. J.; Reinhard, M.; Traina, S. J.; Weber, W. J.; Westall, J. C., Sequestration of Hydrophobic Organic Contaminants by Geosorbents. *Environmental Science & Technology* **1997**, *31*, 3341-3347.
8. Traina, S. J.; Laperche, V., Contaminant Bioavailability in Soils, Sediments, and Aquatic Environments. *Proceedings of the National Academy of Sciences* **1999**, *96*, 3365.
9. Gadd, G. M., Metals, Minerals and Microbes: Geomicrobiology and Bioremediation. *Microbiology* **2010**, *156*, 609-643.

10. Hiemstra, T.; Van Riemsdijk, W. H., On the Relationship between Charge Distribution, Surface Hydration, and the Structure of the Interface of Metal Hydroxides. *Journal of Colloid and Interface Science* **2006**, *301*, 1-18.
11. Henderson, M. A., The Interaction of Water with Solid Surfaces: Fundamental Aspects Revisited. *Surface Science Reports* **2002**, *46*, 1-308.
12. Kelber, J. A., Alumina Surfaces and Interfaces under Non-Ultrahigh Vacuum Conditions. *Surface Science Reports* **2007**, *62*, 271-303.
13. Petitto, S. C.; Tanwar, K. S.; Ghose, S. K.; Eng, P. J.; Trainor, T. P., Surface Structure of Magnetite (111) under Hydrated Conditions by Crystal Truncation Rod Diffraction. *Surface Science* **2010**, *604*, 1082-1093.
14. Ghose, S. K.; Waychunas, G. A.; Trainor, T. P.; Eng, P. J., Hydrated Goethite (α-FeOOH) (100) Interface Structure: Ordered Water and Surface Functional Groups. *Geochimica et Cosmochimica Acta* **2010**, *74*, 1943-1953.
15. Eng, P. J.; Trainor, T. P.; Brown Jr, G. E.; Waychunas, G. A.; Newville, M.; Sutton, S. R.; Rivers, M. L., Structure of the Hydrated α-Al_2O_3(0001) Surface. *Science* **2000**, *288*, 1029.
16. Bargar, J. R.; Brown, G. E.; Parks, G. A., Surface Complexation of Pb(II) at Oxide-Water Interfaces: I. XAFS and Bond-Valence Determination of Mononuclear and Polynuclear Pb(II) Sorption Products on Aluminum Oxides. *Geochimica et Cosmochimica Acta* **1997**, *61*, 2617-2637.
17. Fenter, P.; Sturchio, N. C., Mineral–Water Interfacial Structures Revealed by Synchrotron X-Ray Scattering. *Progress in Surface Science* **2004**, *77*, 171-258.
18. Harmon, K. J.; Chen, Y.; Bylaska, E. J.; Catalano, J. G.; Bedzyk, M. J.; Weare, J. H.; Fenter, P., Insights on the Alumina–Water Interface Structure by Direct Comparison of Density Functional Simulations with X-Ray Reflectivity. *The Journal of Physical Chemistry C* **2018**, *122*, 26934-26944.
19. Chambers, S. A.; Droubay, T.; Jennison, D. R.; Mattsson, T. R., Laminar Growth of Ultrathin Metal Films on Metal Oxides: Co on Hydroxylated α-Al_2O_3(0001). *Science* **2002**, *297*, 827.
20. Niu, C.; Shepherd, K.; Martini, D.; Tong, J.; Kelber, J. A.; Jennison, D. R.; Bogicevic, A., Cu Interactions with α-Al_2O_3(0001): Effects of Surface Hydroxyl Groups Versus Dehydroxylation by Ar-Ion Sputtering. *Surface Science* **2000**, *465*, 163-176.
21. Trainor, T. P.; Eng, P. J.; Brown, G. E.; Robinson, I. K.; Santis, M. D., Crystal Truncation Rod Diffraction Study of the α-Al_2O_3($1\bar{1}02$)Surface. *Surface Science* **2002**, *496*, 238-250.
22. Marmier, A.; Parker, S. C., Ab Initio Morphology and Surface Thermodynamics of α-Al_2O_3. *Physical Review B* **2004**, *69*, 115409.
23. Trainor, T. P.; Chaka, A. M.; Eng, P. J.; Newville, M.; Waychunas, G. A.; Catalano, J. G.; Brown, G. E., Structure and Reactivity of the Hydrated Hematite (0001) Surface. *Surface Science* **2004**, *573*, 204-224.
24. Catalano, J. G.; Park, C.; Zhang, Z.; Fenter, P., Termination and Water Adsorption at the α-Al_2O_3 (012)−Aqueous Solution Interface. *Langmuir* **2006**, *22*, 4668-4673.
25. Tanwar, K. S.; Catalano, J. G.; Petitto, S. C.; Ghose, S. K.; Eng, P. J.; Trainor, T. P., Hydrated α-Fe_2O_3($1\bar{1}02$)Surface Structure: Role of Surface Preparation. *Surface Science* **2007**, *601*, L59-L64.
26. Hass, K. C.; Schneider, W. F.; Curioni, A.; Andreoni, W., The Chemistry of Water on Alumina Surfaces: Reaction Dynamics from First Principles. *Science* **1998**, *282*, 265.
27. Garrity, K. F.; Bennett, J. W.; Rabe, K. M.; Vanderbilt, D., Pseudopotentials for High-Throughput DFT Calculations. *Computational Materials Science* **2014**, *81*, 446-452.
28. Mason, S. E.; Iceman, C. R.; Trainor, T. P.; Chaka, A. M., Density Functional Theory Study of Clean, Hydrated, and Defective Alumina ($1\bar{1}02$) Surfaces. *Physical Review B* **2010**, *81*, 125423.
29. Lo, C. S.; Tanwar, K. S.; Chaka, A. M.; Trainor, T. P., Density Functional Theory Study of the Clean and Hydrated Hematite ($1\bar{1}02$) Surfaces. *Physical Review B* **2007**, *75*, 075425.

30. Mason, S. E.; Iceman, C. R.; Trainor, T. P.; Chaka, A. M., Molecular-Level Understanding of Environmental Interfaces Using Density Functional Theory Modeling. *Physics Procedia* **2010**, *4*, 67-83.
31. Tanwar, K. S.; Lo, C. S.; Eng, P. J.; Catalano, J. G.; Walko, D. A.; Brown, G. E.; Waychunas, G. A.; Chaka, A. M.; Trainor, T. P., Surface Diffraction Study of the Hydrated Hematite ($1\bar{1}02$) Surface. *Surface Science* **2007**, *601*, 460-474.
32. Brown, I. D., Recent Developments in the Bond Valence Model of Inorganic Bonding. *Physics and Chemistry of Minerals* **1987**, *15*, 30-34.
33. Pauling, L., The Principles Determining the Structure of Complex Ionic Crystals. *Journal of the American Chemical Society* **1929**, *51*, 1010-1026.
34. Bargar, J. R.; Towle, S. N.; Brown, G. E.; Parks, G. A., XAFS and Bond-Valence Determination of the Structures and Compositions of Surface Functional Groups and Pb(II) and Co(II) Sorption Products on Single-Crystal α-Al_2O_3 . *Journal of Colloid and Interface Science* **1997**, *185*, 473-492.
35. Mason, S. E.; Iceman, C. R.; Tanwar, K. S.; Trainor, T. P.; Chaka, A. M., Pb(II) Adsorption on Isostructural Hydrated Alumina and Hematite (0001) Surfaces: A DFT Study. *The Journal of Physical Chemistry C* **2009**, *113*, 2159-2170.
36. Ruberto, C.; Yourdshahyan, Y.; Lundqvist, B. I., Surface Properties of Metastable Alumina: A Comparative Study of κ- and α-Al_2O_3 . *Physical Review B* **2003**, *67*, 195412.
37. Verdozzi, C.; Jennison, D. R.; Schultz, P. A.; Sears, M. P., Sapphire (0001) Surface, Clean and with *d*-Metal Overlayers. *Physical Review Letters* **1999**, *82*, 799-802.
38. Wang, X.-G.; Chaka, A.; Scheffler, M., Effect of the Environment on α-Al_2O_3(0001) Surface Structures. *Physical Review Letters* **2000**, *84*, 3650-3653.
39. Toofan, J.; Watson, P. R., The Termination of the α-Al_2O_3(0001) Surface: A LEED Crystallography Determination. *Surface Science* **1998**, *401*, 162-172.
40. Manassidis, I.; De Vita, A.; Gillan, M. J., Structure of the (0001) Surface of α-Al_2O_3 from First Principles Calculations. *Surface Science* **1993**, *285*, L517-L521.
41. Catalano, J. G., Relaxations and Interfacial Water Ordering at the Corundum (110) Surface. *The Journal of Physical Chemistry C* **2010**, *114*, 6624-6630.
42. Kohn, W.; Sham, L. J., Self-Consistent Equations Including Exchange and Correlation Effects. *Physical Review* **1965**, *140*, A1133-A1138.
43. Hohenberg, P.; Kohn, W., Inhomogeneous Electron Gas. *Physical Review* **1964**, *136*, B864-B871.
44. Giannozzi, P., et al., Advanced Capabilities for Materials Modelling with QUANTUM ESPRESSO . *Journal of Physics: Condensed Matter* **2017**, *29*, 465901.
45. Paolo, G., et al., Quantum Espresso: A Modular and Open-Source Software Project for Quantum Simulations of Materials. *Journal of Physics: Condensed Matter* **2009**, *21*, 395502.
46. Perdew, J. P.; Burke, K.; Ernzerhof, M., Generalized Gradient Approximation Made Simple. *Physical Review Letters* **1996**, *77*, 3865-3868.
47. Monkhorst, H. J.; Pack, J. D., Special Points for Brillouin-Zone Integrations. *Physical Review B* **1976**, *13*, 5188-5192.
48. Brese, N. E.; O'Keeffe, M., Bond-Valence Parameters for Solids. *Acta Crystallographica Section B* **1991**, *47*, 192-197.
49. Corum, W. K.; Abbaspour Tamijani, A.; Mason, E. S., Density Functional Theory Study of Arsenate Adsorption onto Alumina Surfaces. *Minerals* **2018**, *8*.
50. Corum, K. W.; Huang, X.; Bennett, J. W.; Mason, S. E., Systematic Density Functional Theory Study of the Structural and Electronic Properties of Constrained and Fully Relaxed (0 0 1) Surfaces of Alumina and Hematite. *Molecular Simulation* **2017**, *43*, 406-419.
51. Tamijani, A. A.; Salam, A.; de Lara-Castells, M. P., Adsorption of Noble-Gas Atoms on the TiO_2(110) Surface: An Ab Initio-Assisted Study with van Der Waals-Corrected DFT. *The Journal of Physical Chemistry C* **2016**, *120*, 18126-18139.

52. Reuter, K., Stampf, C., Scheffler, M., Ab Initio Atomistic Thermodynamics and Statistical Mechanics of Surface Properties and Functions. *Handbook of Materials Modeling* **2005**.
53. Reuter, K.; Scheffler, M., Composition, Structure, and Stability of RuO_2(110)$ as a Function of Oxygen Pressure. *Physical Review B* **2001**, *65*, 035406.
54. Rogal, J., Reuter, K., Ab Initio Atomistic Thermodynamics for Surfaces: A Primer. In Experiment, Modeling and Simulation of Gas-Surface Interactions for Reactive Flows in Hypersonic Flights. *Educational Notes RTO-EN-AVT-142* **2007**, *2*, 18.
55. *NIST-JANAF Thermochemical Tables,*, edited by J.Chase (American Chemical Society, Washington, DC, 1998).
56. Togo, A.; Tanaka, I., First Principles Phonon Calculations in Materials Science. *Scripta Materialia* **2015**, *108*, 1-5.
57. Huang, X.; Ramadugu, S. K.; Mason, S. E., Surface-Specific DFT + U Approach Applied to α-Fe_2O_3(0001). *The Journal of Physical Chemistry C* **2016**, *120*, 4919-4930.
58. Mason, S. E.; Trainor, T. P.; Chaka, A. M., Hybridization-Reactivity Relationship in Pb(II) Adsorption on α-Al_2O_3-Water Interfaces: A DFT Study. *The Journal of Physical Chemistry C* **2011**, *115*, 4008-4021.
59. Chen, Y.; Bylaska, E. J.; Weare, J. H., Weakly Bound Water Structure, Bond-Valence Saturation and Water Dynamics at the Goethite (100) Surface/Aqueous Interface: Ab Initio Dynamical Simulations. *Geochemical Transactions* **2017**, *18*, 3.
60. Hoffmann, R., A Chemical and Theoretical Way to Look at Bonding on Surfaces. *Reviews of Modern Physics* **1988**, *60*, 601-628.
61. Bargar, J. R.; Towle, S. N.; Brown, G. E.; Parks, G. A., Outer-Sphere Pb(II) Adsorbed at Specific Surface Sites on Single Crystal α-Alumina. *Geochimica et Cosmochimica Acta* **1996**, *60*, 3541-3547.
62. Mason, S. E.; Corum, K. W.; Ramadugu, S. K., Fundamental Insights About Environmental Interface Reactivity from DFT Calculations of Geochemical Model Systems. *Surface Science* **2015**, *631*, 48-56.
63. Ramadugu, S. K.; Mason, S. E., Dft Study of Antimony(V) Oxyanion Adsorption on α-$Al_2O_3(1\bar{1}02)$. *The Journal of Physical Chemistry C* **2015**, *119*, 18149-18159.